RSC Applied Polymers

ROYAL SOCIETY OF CHEMISTRY

PAPER

View Article Online
View Journal | View Issue

Cite this: *RSC Appl. Polym.*, 2026, **4**, 689

Harnessing 1,8-Naphthalimide based amide capped with Pluronic F127 micelles for the detection of chlorpyrifos methyl and erythrosine B

Nisha Jain and Navneet Kaur *

Considering the detrimental effects of chlorpyrifos methyl (CPS methyl) and erythrosine B on living organisms, it is crucial to detect their presence even at trace levels. For this, a binary ensemble, **NPOH@PF127**, was developed by encapsulating the 1,8-naphthalimide-based amide **NPOH** in the hydrophobic core of micelles of the block copolymer Pluronic F127. Structural and chemical properties of this binary ensemble were scrupulously investigated using various analytical techniques such as DLS, HRTEM, EDX, elemental mapping, SAED, PXRD, FT-IR spectroscopy, TGA, DSC, DTG, XPS and optical spectroscopy. The sensor exhibited significant enhancement and quenching of fluorescence intensity upon interaction with CPS methyl (LOD = 1.28 μM) and erythrosine B (LOD = 0.18 μM), respectively, with corresponding linear detection ranges of 4.22–1500 μM and 0.59–138 μM. Moreover, **NPOH@PF127** accurately detected CPS methyl and erythrosine B in grape juice and watermelon juice, with excellent recoveries in the range of 96% to 110%. Given the high stability, quick response, high sensitivity and selectivity of **NPOH@PF127**, it can be utilized for making portable test kits and thus contribute to refined environmental and food safety monitoring.

Received 15th September 2025,
Accepted 2nd January 2026

DOI: 10.1039/d5lp00287g

rsc.li/rscapplpolym

1. Introduction

Organophosphorus pesticides, esters of phosphoric acid derivatives, have been designated as pivotal crop defensive agents due to their high efficacy for pest control; however, their overuse has become a serious global concern in recent years due to their severe harmful effects on the human health and environment because of their ability to leave residues and contaminants on various agricultural products they are being sprayed or sprinkled upon.[1] CPS methyl is an extensively used non-systemic organophosphate pesticide, which is effective against bollworm, leafhopper, aphid, mite and a variety of other pests.[2] CPS methyl has been classified as a class II moderate toxicity pesticide by the World Health Organization (WHO) and is found in one-third of conventionally grown citrus fruits.[2] Long-term exposure of food commodities to CPS methyl may lead to increased chances of their entry into the food chain and thus cause serious ailments in living organisms.[3] In humans, CPS methyl undergoes complexation with the active site of the neuroenzyme acetylcholinesterase, leading to inhibition in its activity in erythrocytes and the brain, causing adverse effects on the nervous system. Other detrimental effects caused by CPS methyl include oxidative stress, cardiovascular diseases, endocrine disruption, hematological malignancies, histopathological aberrations, immunotoxicity, genotoxicity and developmental and behavioural anomalies.[4] Considering its high toxicity, many governments have made efforts to limit its application in farming by assigning a maximum residue limit (MRL).[5]

It is an age-old practice to add food colorants to food products in order to make them visually appealing to customers. The origin of food colorants can be natural or synthetic; however, synthetic colorants are preferred over the natural ones as the former are easy to synthesize, cost-effective, highly stable and offer potent tinting.[6] Erythrosine B (2-(6-hydroxy-2,4,5,7-tetraiodo-3-oxo-xanthen-9-yl) benzoic acid), a pink polyiodinated xanthene dye, is globally added to food products, pharmaceuticals and cosmetics as it has high antioxidant potential and stability and low cost.[7] However, due to its polyhalogenated structure, immoderate consumption of erythrosine B causes many health risks such as behavioural disturbances, allergies, renal disorders, thyroid disorders, asthma, bronchitis, hemolytic disorder, anemia, cancer, DNA damage and neurotoxicity in humans and animals. Moreover, the health issues are more pronounced in children as their bodies are weaker as compared to adults.[8] Keeping in mind the adverse effects of the excessive use of erythrosine B, the Food and Drug Administration (FDA) has restricted its consumption

Department of Chemistry, Panjab University, Chandigarh 160014, India.
E-mail: neet_chem@yahoo.co.in, neet_chem@pu.ac.in; Fax: +91172 2545074;
Tel: +91 172 2534430

to an acceptable daily intake (ADI) of 0.0–0.1 mg per kg body weight per day.[9]

Bearing in mind the notorious effects of CPS methyl and erythrosine B on living beings, it is essential to detect them even at minute levels. Already existing techniques for their detection include chromatographic techniques, such as high-performance liquid chromatography (HPLC), gas chromatography (GC), and other techniques like surface enhanced Raman spectroscopy (SERS), electrochemical method, photoelectrochemical method, immunosensor method, ion mobility spectroscopy, mass spectrometry, nuclear quadruple resonance spectroscopy, capillary electrophoresis (CE) and solid phase extraction (SPE).[10–21] Undoubtedly, these techniques may achieve high detection sensitivities, but these generally involve bulky instrumentation, exorbitant methodologies, multiple sample processing steps, professional operators and longer analysis time. These shortcomings make them difficult to meet the high-throughput, rapid and on-site detection requirements.[22] Optical spectroscopic techniques, such as UV-vis and fluorescence spectroscopy, are beneficial over the aforementioned techniques as these are comparatively simple to operate, cost-effective and offer rapid visual response with high sensitivity and selectivity.[23–25]

Many optical sensors, such as organic compounds, molecularly imprinted polymers, metal nanoparticles, carbon dots, and organic nanoparticles, have been employed for the detection of organophosphate pesticides; however, a very limited number of optical chemosensors have been reported for the sensing of erythrosine B.[26–29] Among these, organic compound-based sensors are of significant importance as they are structurally versatile and it is easier to modify their photophysical properties by slight structural changes.[30] But the major issue associated with organic compound-based sensors is their limited applicability in aqueous medium (a prerequisite for real sample analysis) due to their hydrophobic nature.[31] Some of the efforts by various researchers over the years to enhance the hydrophilicity of organic compounds include encapsulation of organic compounds in the hydrophobic core of micelles of suitable materials, such as surfactants and polymers, formation of small molecule-based organic nanoparticles and silica cross-linked micellar nanoparticles.[32–35] Among the various materials used for the encapsulation of organic compounds, Pluronic F127 (**PF127**), a Food and Drug Administration (FDA) approved non-ionic block copolymer, has garnered significant attention as it is non-toxic, non-irritant, biocompatible, thermo reversible and cost effective.[36] **PF127** is a triblock copolymer consisting of hydrophobic polypropylene oxide (PPO) as the central unit and hydrophilic polyethylene oxide (PEO) as two terminal units.[37] In aqueous environments, **PF127** spontaneously forms nanoscale micelles, with the hydrophobic PPO segments creating the inner core for loading hydrophobic molecules, while the hydrophilic PEO chains stabilize the outer shell and prevent micelle coalescence.[38] Apart from improving solubility, encapsulating sensors in **PF127** micelles offers several advantages over their free forms. The micellar environment supports hydrophobic probes by preventing aggregation, enhancing colloidal stability, protecting against premature degradation to improve photostability, and reducing cytotoxicity for safer biological use.[39–41] Moreover, the nanoscale micellar structure provides a high surface-to-volume ratio, improved diffusion kinetics, and a confined hydrophobic core, facilitating efficient probe–analyte interactions, reducing background interference, and enhancing sensitivity, reproducibility, and overall sensor performance compared to free systems. Additionally, the small size of nanoscale micelles and the stealth properties of the PEO corona prolong the circulation time and allow passive tumor targeting *via* the enhanced permeability and retention effect, making encapsulated sensors more suitable for bioimaging and *in vivo* sensing applications.[42–44] Collectively, these features make **PF127**-encapsulated sensors more sensitive, stable, and versatile than their free molecular counterparts.

In this work, a 1,8-naphthalimide-based amide (**NPOH**) was synthesized considering the well-known photophysical advantages of the 1,8-naphthalimide core, including red/infrared emission, large Stokes shift, high quantum yield, and strong two-photon absorption cross-section.[45] To overcome its intrinsic hydrophobicity, a binary ensemble, **NPOH@PF127**, was fabricated by encapsulating **NPOH** within the hydrophobic core of **PF127** micelles. This hybrid design combines the tunable fluorescence and sensing versatility of naphthalimide dyes with the biocompatibility, aqueous solubilization, and self-assembly properties of **PF127**. Unlike conventional 1,8-naphthalimide sensors used mainly in homogeneous media or polymer matrices, the **PF127** micellar environment enhances solubility, stability, and microenvironment-induced modulation of fluorescence.[45] Conversely, while **PF127** is widely employed for solubilization and drug delivery, it inherently lacks sensing capability; loading **NPOH** introduces strong, responsive fluorescence into the platform. As a result, the **NPOH@PF127** ensemble exhibits improved optical performance, high sensitivity and selectivity, and reliable operation in aqueous media, enabling effective differential sensing of CPS methyl and erythrosine B in grape and watermelon juices, respectively. This synergistic integration offers sensing advantages unattainable with either component alone and represents a hybrid approach for real sample analysis.

2. Experimental

2.1. Materials

All chemicals, such as 4-bromo-1,8-naphthalic anhydride, *N*-butyl amine, ethylene diamine, 1-hydroxy-2-naphthoic acid, 1-[bis(dimethylamino)methylene]-1*H*-1,2,3-triazolo[4,5-*b*]pyridinium 3-oxide hexafluorophosphate (HATU), Pluronic F-127 (**PF127**), 4-(2-hydroxyethyl)piperazine-1-ethanesulfonic acid (HEPES), chloroform, dichloromethane (DCM), anhydrous sodium sulfate, ethanol (EtOH), methanol, dimethyl sulfoxide (DMSO), acetonitrile (ACN), pyridine, CPS methyl, glufosinate, glyphosate, imidacloprid, malathion, paraquat, thiomethoxam,

diethyl chlorophosphate (DCP), diethyl cyanophosphonate (DCNP), triphosgene, erythrosine B, Allura red, amaranth, methylene blue, methyl orange, glucose, sucrose, lactose, maltose, citric acid, ascorbic acid, sodium chloride (NaCl), salts of metal ions and anions *viz*. Cd^{2+}, Co^{2+}, Mn^{2+}, Pb^{2+}, Cr^{3+}, HSO_4^-, ClO_4^-, $H_2PO_4^-$, SO_4^{2-}, F^-, Cl^-, Br^- and I^-, were purchased from commercial suppliers and were used without any further purification.

2.2. Methods

High-resolution transmission electron microscopy (HRTEM). For recording HRTEM images, elemental mapping and selected area electron diffraction (SAED) patterns, the HRTEM-Hitachi H7500 electron microscope was employed. Samples were drop-cast on carbon-coated copper grids and air-dried prior to imaging.

Energy dispersive X-ray (EDX) spectroscopy. EDX spectroscopy was recorded using a FESEM-Hitachi SU8010 at an accelerating voltage of 15 kV. For EDX measurements, samples were mounted on an aluminium SEM stub using double-sided carbon adhesive tape, followed by gold sputter-coating prior to analysis.

Dynamic light scattering (DLS). To obtain the hydrodynamic diameter, DLS measurements were performed on a Malvern Zetasizer (Ver. 7.11) at 25 °C using water as the dispersion medium, and samples were filtered through a 0.2 μm syringe filter before measurement. Each sample was analyzed in triplicate to ensure reproducibility.

Nuclear magnetic resonance (NMR) and Fourier transform infrared (FT-IR) spectroscopies. ^{1}H and ^{13}C NMR spectra were recorded on a Bruker AVANCE NEO 500 MHz spectrometer using DMSO-d_6 or $CDCl_3$ as a solvent, depending on the solubility of the compounds. Chemical shifts are reported in ppm relative to TMS, and spectra were acquired at 298 K. FT-IR spectra were obtained using a Bruker Alpha FT-IR spectrophotometer in the ATR mode with a spectral range of 4000–400 cm^{-1}.

Mass spectrometry. High-resolution mass spectrometry (HRMS) and liquid chromatography-mass spectrometry (LC-MS) analyses were performed on a SYNAPT XS instrument operated in ESI (positive) mode.

X-ray diffraction studies. Powder X-ray diffraction (PXRD) patterns were acquired on an Empyrean diffractometer (Malvern Panalytical) using Cu-Kα radiation (λ = 1.5406 Å), operated at 40 kV and 40 mA, with a scan rate of 0.02° s^{-1} over the 2θ range of 5–80°.

Thermal studies. Thermogravimetric analysis (TGA), differential thermogravimetric analysis (DTG) and differential scanning calorimetry (DSC) were conducted using an SDT Q600 V20.9 Build 20 instrument under nitrogen atmosphere (flow rate: 50 mL min^{-1}) at a heating rate of 10 °C min^{-1} from 25 to 800 °C.

X-ray photoelectron spectroscopy (XPS) measurements. X-ray photoelectron spectroscopy (XPS) measurements were carried out on a Nexsa Base Thermo Fisher Scientific instrument using monochromatic Al Kα radiation (1486.6 eV). All spectra were charge-corrected using the C 1s peak at 284.8 eV.

Optical studies. UV–vis absorption spectra were recorded using a JASCO UV-750 spectrophotometer with samples prepared in aqueous medium using quartz cuvettes (1 cm path length) at 25 °C. Fluorescence spectra were recorded on a Hitachi F-7000 spectrofluorometer equipped with a 220–240 V xenon lamp, with excitation and emission slit widths typically set to 5 and 10 nm, respectively.

Fluorescence lifetime studies. Fluorescence lifetime measurements were performed using an Edinburgh FLS-1000-XS-T spectrometer. Samples were measured in a standard holder suitable for liquid samples, and lifetime data were acquired using time-correlated single photon counting (TCSPC) mode and processed using the instrument's software.

2.3. Synthesis of NPOH

Compounds **2** and **3** were synthesized as per the previously reported methodologies,[46,47] with modifications shown in Scheme 1. Methods for the synthesis of **1** and **2**, their characterization data and spectra (^{1}H NMR, ^{13}C NMR and LCMS) are given in SI as Fig. S1–S6.

Synthesis of *N*-(2-((2-butyl-1,3-dioxo-2,3-dihydro-1*H*-benzo[*de*]isoquinolin-6-yl)amino)ethyl)-1-hydroxy-2-naphthamide, NPOH. A mixture of 1-hydroxy-2-naphthoic acid (0.3 g, 1.6 mmol) and HATU (0.7 g, 1.9 mmol) in pyridine (10 mL) was stirred at 0 °C for 30 min. Further, compound **3** (0.5 g, 1.6 mmol) was added to the reaction mixture, and stirring was carried out at room temperature. After completion of the reaction (24 h), the reaction mixture was poured into water and extracted with chloroform (3 × 100 mL). The organic layer was dried over anhydrous sodium sulfate and concentrated under reduced pressure. The crude product thus obtained was washed with methanol to get the pure product, **NPOH**. Yellow solid; 87% yield; m.p. (°C) = 390–394; ^{1}H NMR (500 MHz, DMSO-d_6) δ ppm: 14.46 (s, 1H, –OH), 9.22 (s, 1H, –NH amide), 8.65 (d, 1H, Ar–H, J = 8.0 Hz), 8.44 (d, 1H, Ar–H, J = 6.95 Hz), 8.31–8.26 (m, 2H, Ar–H), 7.95 (s, 1H, –NH), 7.86 (d, 1H, Ar–H, J = 8.1 Hz), 7.83 (d, 1H, Ar–H, J = 8.9 Hz), 7.70 (t, 1H, Ar–H, J_1 = 7.95 Hz, J_2 = 7.75 Hz), 7.63 (t, 1H, Ar–H, J_1 = 7.0 Hz, J_2 = 7.55 Hz), 7.55 (t, 1H, Ar–H, J_1 = 7.5 Hz, J_2 = 7.3 Hz), 7.38 (d, 1H, Ar–H, J = 10.75 Hz), 6.96 (d, 1H, Ar–H, J = 8.6 Hz), 4.01 (t, 2H, $-CH_2$, J_1 = 7.35 Hz, J_2 = 7.45 Hz), 3.68 (s, 4H, 2 × $-CH_2$), 1.62–1.56 (m, 2H, $-CH_2$), 1.37–1.30 (m, 2H, $-CH_2$), 0.92 (t, 3H, $-CH_3$, J_1 = 7.35 Hz, J_2 = 7.4 Hz); ^{13}C NMR (500 MHz, DMSO-d_6) δ ppm: 170.81, 163.61, 162.79, 150.43, 135.71, 134.01, 129.30, 128.71, 128.36, 127.32, 125.62, 124.29, 122.91, 121.91, 120.14, 107.89, 106.93, 103.68, 29.71, 19.71, 13.63; FT-IR (cm^{-1}): 3461 ($\nu_{O-H\ str.}$), 3334 ($\nu_{N-H\ str.}$), 3038 ($\nu_{C-H\ str.}$, aromatic), 2933 ($\nu_{=C-H\ str.}$), 2840 ($\nu_{C-H\ str.}$, aliphatic), 1755 ($\nu_{C=O\ str.}$), 1657 ($\nu_{C=N\ str.}$), 1344 ($\nu_{C-N\ str.}$); HRMS: m/z calculated for $C_{29}H_{27}N_3O_4$ [M^+] = 481.55, found = 482.20 [M + H^+]. ^{1}H NMR, ^{13}C NMR, FT-IR and HR-MS spectra of **NPOH** have been displayed in Fig. S7–S10.

2.4. Synthesis of NPOH@PF127

A mixture of **NPOH** (2 mg) and **PF127** (80 mg) in 10 mL DCM was sonicated for 20 min, followed by solvent evaporation under reduced pressure. The product so obtained was dried in

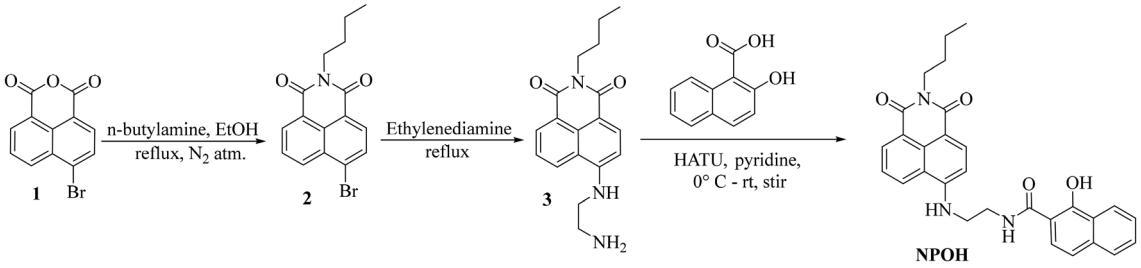

Scheme 1 Protocol for the synthesis of **NPOH**.

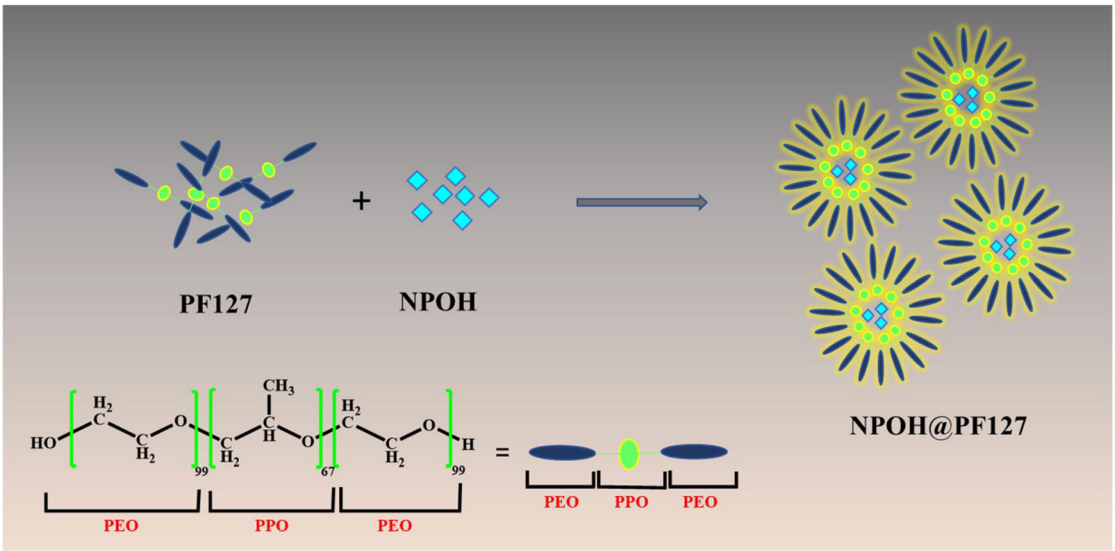

Fig. 1 Protocol for the synthesis of **NPOH@PF127**.

a desiccator for 12 h, hydrated with 10 mL deionized water and sonicated for 20 min (Fig. 1). The solution was then filtered through a 0.2 μm filter to remove unloaded **NPOH**.[37] The **NPOH@PF127** dispersed in HEPES buffer (10 mM, pH = 7.0) or freeze-dried solid was used for further characterization and application. HEPES buffer, which is effective in providing stable conditions in the near neutral pH range (7.0–7.2), was selected owing to its non-toxic nature, robust pH stability at working concentrations and chemically inert environment. In contrast to PBS, HEPES exhibits markedly lower ionic interference, minimal background fluorescence and enhanced nanomaterial stability, thereby offering clear advantages for sensitive optical and nanomaterial-based sensing.[48–50]

2.5. Preparation of samples

A 0.01 M stock solution of **NPOH** in DMSO and 0.01 M stock solutions of CPS methyl, glufosinate, glyphosate, imidacloprid, malathion, paraquat, and thiamethoxam were prepared in EtOH. 0.1 M stock solutions of DCP, DCNP, triphosgene and tetrabutylammonium salts of anions (HSO_4^-, ClO_4^-, $H_2PO_4^-$, SO_4^{2-}, F^-, Cl^-, Br^-, and I^-) were prepared using ACN. 5 mM stock solutions of food dyes (erythrosine B, Allura red, amaranth, methylene blue, methyl orange), 0.1 M stock solutions of metal ions (Cd^{2+}, Co^{2+}, Mn^{2+}, Pb^{2+}, and Cr^{3+}), sugars (glucose, sucrose, lactose, and maltose), citric acid and ascorbic acid were prepared in deionized water. Aliquots of these analytes were added to the 2 mL solution of **NPOH@PF127**, and spectroscopic scans were recorded.

2.6. Real sample analysis

To evaluate the practical utility of the proposed sensor **NPOH@PF127**, it was utilized for the detection of CPS methyl and erythrosine B in grape juice and watermelon juice. The juice was extracted from the pulp of fresh grapes and watermelon samples, followed by centrifugation to remove the coarse pulp and insoluble matter. The juices were then diluted 10 times with deionized water to reduce matrix complexity, decrease viscosity and minimise interference from endogenous pigments and polyphenols. The diluted samples were then adjusted to pH 7.0 to match the optimised sensing conditions of **NPOH@PF127** and subsequently filtered through a 0.22 μm membrane to eliminate residual particulates. The filtered grape and watermelon juice samples were spiked with CPS methyl (50, 800, 1500 μM) and erythrosine B (4, 15, 60 μM), respectively. Then, 50 μL aliquots of

these samples were used for further analysis. Background fluorescence was evaluated using unspiked juice blanks, which showed negligible emission in the detection window of **NPOH@PF127**, indicating that endogenous juice components did not interfere with the probe's fluorescence response. These steps ensured efficient suppression of matrix effects and enabled reliable quantification of CPS methyl and erythrosine B in fruit juice samples. To calculate percent recovery values, the following formula was used.

$$\text{Recovery}\ (\%) = (\text{Intensity of emission peak in the real sample medium}/\text{intensity of emission peak in deionized water}) \times 100$$

3. Results and discussion

3.1. Characterization of NPOH@PF127

The dimensions and morphological features of **NPOH@PF127** were examined using DLS and HRTEM techniques. From DLS results (Fig. S11), the hydrodynamic radius of **NPOH@PF127** was found to be 24.24 nm. HRTEM images (inset (Fig. 2b)) clearly showed the **NPOH** molecules encapsulated inside the core of spherical micelles formed by the **PF127** polymer. The average particle size of the prepared binary ensemble was determined from the HRTEM micrograph (Fig. 2a) using ImageJ software and was found to be 11.05 ± 2.21 nm, along with the presence of lattice fringes of 0.33 nm over its surface (Fig. 2c). The particles appeared to be monodispersed and spherical in shape, showing no visible agglomeration. Particle diameters were measured from the HRTEM images using ImageJ software, where the scale bar was used to calibrate the pixel-to-nanometer conversion and the diameters of 24 individual particles were averaged to obtain the mean particle size using the following formula:

$$D = \frac{1}{N}\sum_{i=1}^{N} d_i$$

The observed difference between the sizes obtained from DLS and TEM measurements may be attributed to the fact that DLS measures the hydrodynamic diameter of particles in aqueous solution, including the solvation shell, any adsorbed **PF127** polymer or other surface layers and potential small aggregates, whereas TEM measures the physical core size after drying, under high vacuum.[51,52] The elemental composition of **NPOH@PF127** was determined using EDX analysis (Fig. 2e), which revealed the presence of C, N and O with the atomic percentages of 67.65%, 31.22% and 1.13%, respectively. Further, elemental mapping results (Fig. 2f–i) also demonstrated the uniform distribution of all the aforementioned required elements with carbon, nitrogen and oxygen shown in pink, red and green colors, respectively.

In the selected-area electron diffraction (SAED) pattern (Fig. 2d) of **NPOH@PF127**, diffraction spots were observed, which gave a hint towards its crystalline nature, which corroborated well with XRD results. The highly crystalline nature of **NPOH@PF127** was confirmed by the intense diffraction peaks at 2θ = 19.20° and 23.32°, which corresponded to the (220) and (311) lattice planes of the PEO block in Pluronic F127 (Fig. S12).[53] Moreover, it is worth mentioning that the diffractograms of **NPOH**, **PF127** and **NPOH@PF127** (Fig. S12) showed highly crystalline patterns, and the diffractogram of **NPOH@PF127** was found to be exactly similar to PF127, indicating complete encapsulation of **NPOH** inside PF127 micelles.[37,54]

Further, FT-IR spectra of **NPOH**, **PF127** and **NPOH@PF127** were recorded. As shown in Fig. S13a, in the FT-IR spectrum of **NPOH**, absorption peaks were observed at 1344, 1657, 1755, 2840, 2933, 3038, 3334 and 3439 cm^{-1}, due to stretching vibrations of C–N, C═N, C═O, C–H aliphatic, ═C–H, C–H aromatic, N–H and O–H groups, respectively. In the FT-IR spectrum of **PF127** (Fig. S13b), characteristic absorption peaks due to stretching vibrations of C–O, C–O–C, C–H–C and C–H appeared at 1101, 1279, 1458 and 2878 cm^{-1}, respectively, and the absorption peak due to bending vibrations of O–H appeared at 1342 cm^{-1}. From the comparison of the FT-IR spectra of **NPOH**, **PF127** and **NPOH@PF127** (Fig. S13), it was found that the FT-IR spectrum of **NPOH@PF127** is similar to that of free **PF127**, indicating that **NPOH** molecules are encapsulated in the hydrophobic core of **PF127** micelles through physical interactions.[54]

To further explore the chemical composition of **NPOH** and **NPOH@PF127**, their XPS spectra were obtained. As shown in Fig. 3a and e, signals corresponding to binding energies of C 1s, N 1s and O 1s were observed in the survey spectra of both **NPOH** and **NPOH@PF127**. In the high-resolution deconvoluted XPS spectrum of C 1s of **NPOH** (Fig. 3b), binding energy peaks at 284.68, 286.26 and 288.76 eV confirmed the presence of C–C/C═C, C–O/C–N and C═O, respectively.[55] The presence of NH in **NPOH** was ascertained by the presence of the binding energy peak at 399.62 eV (Fig. 3c) in the core level spectra of N 1s.[55] The high-resolution spectra of O 1s of **NPOH** (Fig. 3d) displayed a binding energy peak at 532.53 eV corresponding to C–OH.[55] Similar peaks were observed in the high-resolution deconvoluted spectra of C 1s, N 1s and O 1s of **NPOH@PF127** (Fig. 3f–h) except for the disappearance of the binding energy peak corresponding to C═O, which may be due to its involvement in interaction with **PF127**. Moreover, considerable differences in the intensity of binding energy peaks of C–O/C–N, N–H, and C–OH in **NPOH** and **NPOH@PF127** also pointed to their involvement in chemical interactions between **NPOH** and **NPOH@PF127**.[56]

Further, from XPS analysis, the elemental composition of **NPOH** was found to be C (85.5%), N (0.67%) and O (13.83%), whereas **NPOH@PF127** displayed C (83.7%), N (0.2%) and O (16.1%). Thus, the encapsulation of **NPOH** in **PF127** micelles increased the content of surface atomic oxygen from 13.83% to 16.1%, indicating enrichment of the ether (–C–O–) groups of **PF127** at the outermost surface. Decrement in the atomic nitrogen percentage from 0.67% to 0.2% pointed towards the encapsulation of nitrogen-containing **NPOH** within the hydrophobic core of micelles formed by **PF127**.

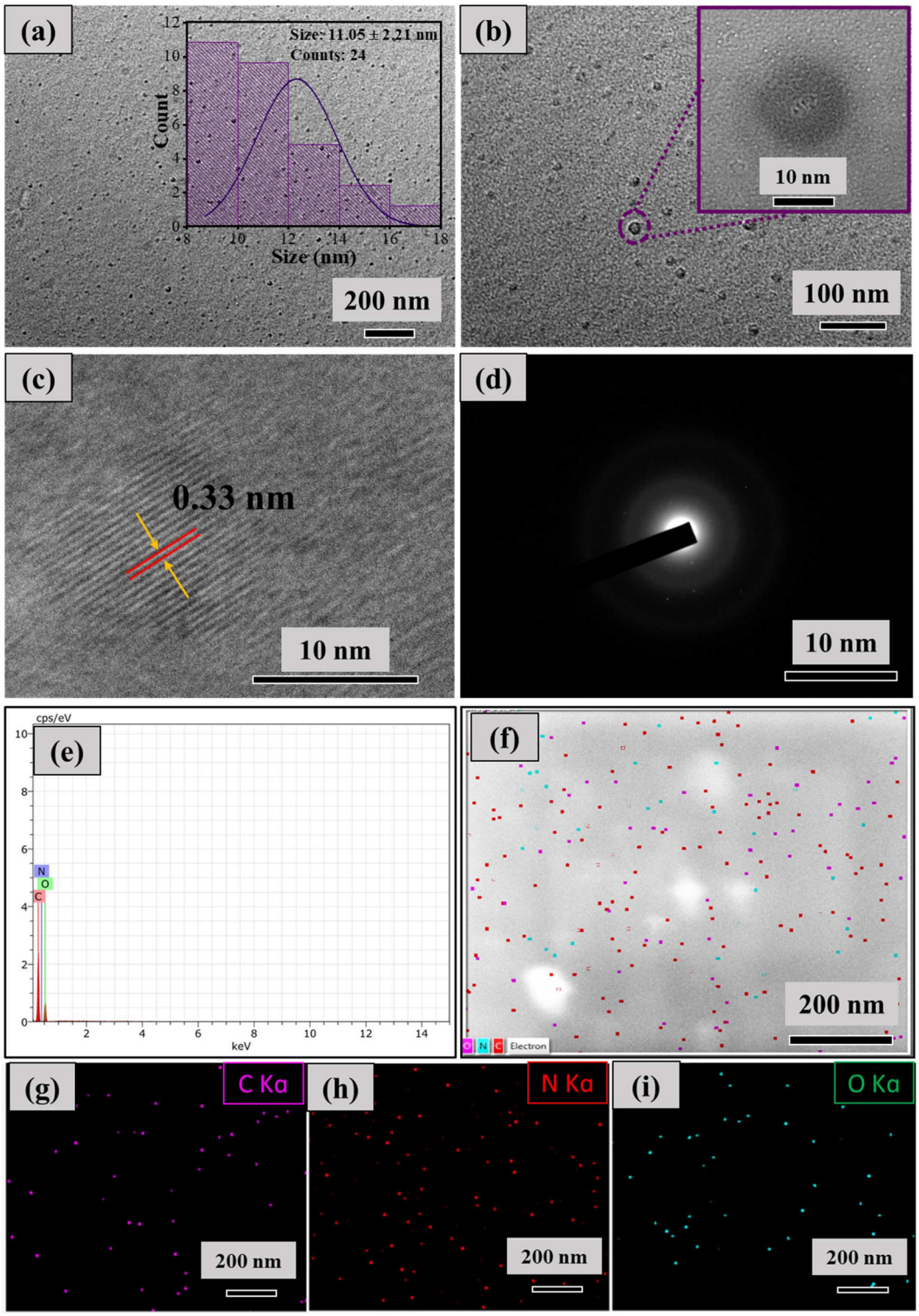

Fig. 2 (a–c) HRTEM images, (d) SAED pattern, (e) EDX spectra, and (f–i) elemental mapping of **NPOH@PF127**; inset (a): size distribution graphs of the counts obtained from the HRTEM image (a); inset (b): HRTEM image of a single particle of **NPOH@PF127**.

To evaluate thermal stability and confirm the formation of the binary ensemble **NPOH@PF127**, comparison of TGA, DTG and DSC curves of **NPOH**, **PF127** and **NPOH@PF127** was carried out (Fig. S14). As shown in Fig. S14a, in the case of **NPOH@PF127**, a weight loss of 11.18% occurred in the temperature range of 30–313 °C, while for **PF127** and **NPOH**, the weight loss was found to be only 2.15% and 0.53%, respectively. In the temperature range of 313–800 °C, the weight loss

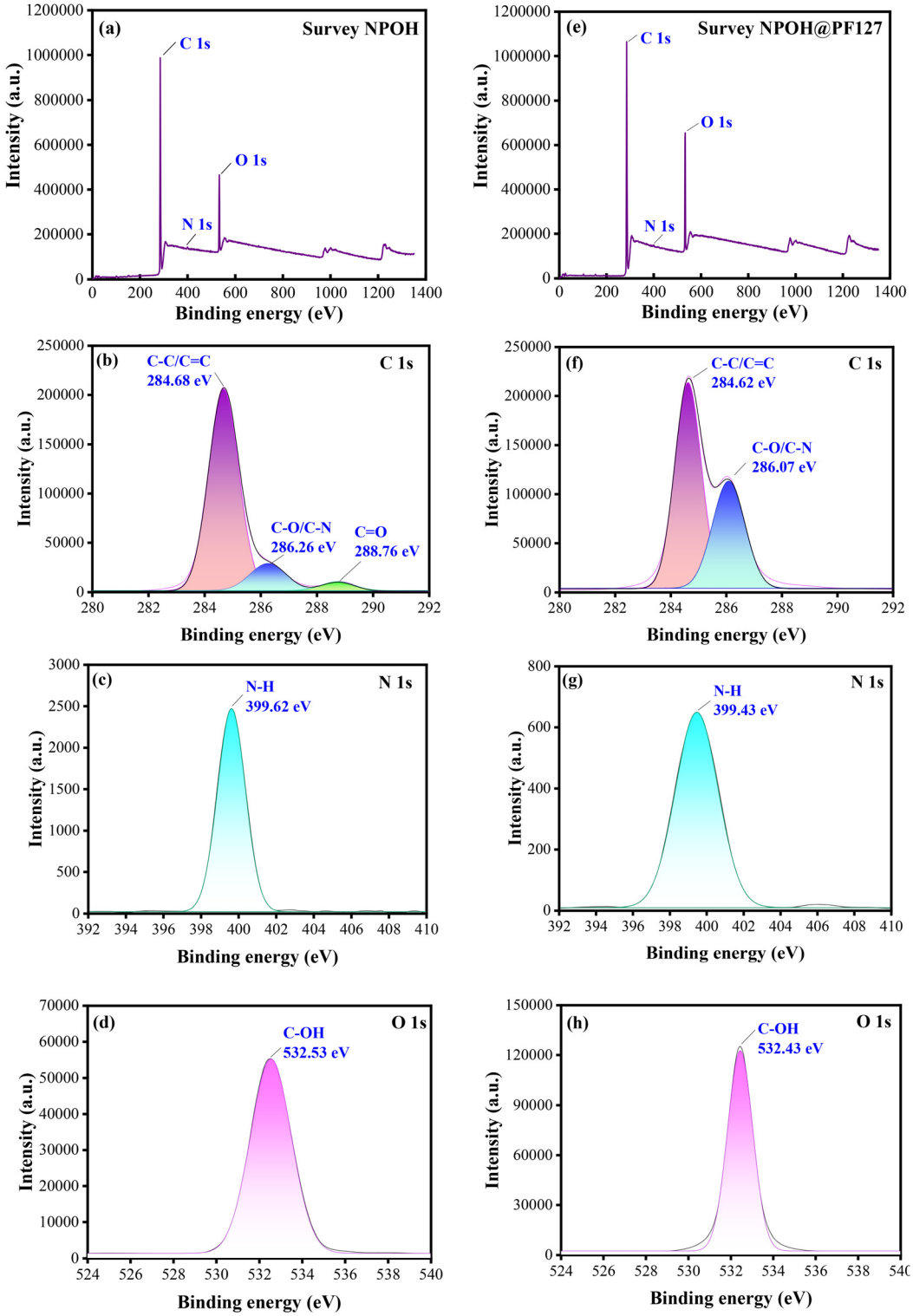

Fig. 3 XPS survey scan of (a) **NPOH** and (e) **NPOH@PF127**. Deconvoluted spectra of C (1s), N (1s) and O (1s) for **NPOH** (b–d) and **NPOH@PF127** (f–h).

for **NPOH**, **PF127** and **NPOH@PF127** was found to be 108.9%, 97.01% and 96.76%, respectively, which indicated higher thermal stability of **NPOH@PF127** than the individual components.[57] From the DTG curves (Fig. S14b), maximum weight loss in the case of **NPOH**, **PF127** and **NPOH@PF127** occurred at 372.21–393.68 °C, 401.85 °C and 406.61 °C, respectively. Thus, the decomposition temperature of **NPOH@PF127** was found to be higher than both individual components, which

again indicated higher stability of **NPOH@PF127**.[58] In the DSC curves (Fig. S14c), endothermic peaks at 303.03 °C, 300.83 °C and 306.44 °C refer to the temperature at which the dehydration of **NPOH**, **PF127** and **NPOH@PF127** occurs while the endothermic peaks at 387.65 °C, 403.03 °C and 410.12 °C indicate their melting temperatures. Thus, amongst all, the highest melting temperature was observed for **NPOH@PF127**, indicating its high stability.[59,60] Additionally, the difference in the thermal stability of **NPOH@PF127** in comparison to the individual components validated the successful formation of the binary ensemble.

3.2. Optical studies of NPOH and NPOH@PF127

UV-vis and fluorescence spectroscopic techniques were employed to evaluate the optical properties of **NPOH** and **NPOH@PF127**. The UV-vis absorption spectrum of **NPOH** (8 μM) in HEPES buffer (10 mM, pH = 7.0) displayed two absorption bands, one high-energy band at 357 nm and another low-energy band at 455 nm (Fig. 4a).[61] The absorption peak at 357 nm was assigned to the $\pi \rightarrow \pi^*$ transition of the aromatic ring, whereas the band observed at 455 nm was attributed to the intramolecular charge-transfer (ICT) transition from the aromatic ring to the 1,8-naphthalimide moiety.[62] In aqueous medium, **NPOH** exhibited comparatively lower absorption intensity, which can be attributed to extensive hydrogen bonding with water molecules and the formation of π–π stacked aggregates, both of which induce hypochromism and spectral broadening.[63,64] Upon comparison of the UV-vis absorption spectrum of **NPOH@PF127** (**NPOH** = 8 μM, **PF127** = 12 μM) with **NPOH** (8 μM) in HEPES buffer (10 mM, pH = 7.0), it was found that in the case of **NPOH@PF127**, there was considerable enhancement in the intensity of both the absorption bands, along with their splitting in two bands and new bands appeared at 446, 424, 356 and 343 nm (Fig. 4a). This enhancement arises from the efficient solubilization of **NPOH** within the hydrophobic core of **PF127**, which minimizes water-induced hydrogen bonding and effective suppression of π–π aggregation, thereby stabilizing **NPOH** in a monomeric state. The micellar microenvironment thus facilitates more efficient $\pi \rightarrow \pi^*$ electronic transitions and sharper $n \rightarrow \pi^*$ features due to reduced polarity and restricted non-radiative interactions. Overall, the stronger and better-defined absorption bands of **NPOH@PF127** confirm the successful encapsulation and creation of a more favorable photophysical environment for the dye.[65,66]

To further support the encapsulation of **NPOH** in polymeric micelles, fluorescence spectroscopic measurements were carried out. Upon excitation at 450 nm, **NPOH** (60 μM) in HEPES buffer (10 mM, pH = 7.0) showed only faint fluorescence with a low-intensity emission peak at 542 nm, which might be due to the aggregation-caused quenching (ACQ) effect of the aggregates of **NPOH** molecules formed in the aqueous medium.[67]

Meanwhile, in the emission spectrum of **NPOH@PF127** (**NPOH** = 60 μM, **PF127** = 90 μM), a blue-shifted (18 nm) and intense emission peak was observed at 524 nm, indicating its highly emissive nature (Fig. 4b). This change may be attributed to changes in the microenvironment and aggregation states upon the encapsulation of **NPOH** molecules in polymeric micelles.[68] Upon incorporation into **PF127** micelles, the probe experiences a more ordered and less polar microenvironment that restricts intermolecular interactions and suppresses aggregation. This microencapsulation effectively isolates individual **NPOH** molecules, resulting in sharper absorption features and enhanced fluorescence intensity. Further, the fluorescence decay profiles of free **NPOH** and its binary ensemble **NPOH@PF127** were recorded, and the corresponding decay curves are presented in Fig. S15. Upon the encapsulation of **NPOH** into **PF127** micelles, the fluorescence lifetime increased from 5.45 to 5.53 ns. This slight enhancement may be ascribed to the more restricted, hydrophobic microenvironment offered by the micellar core, which shields the fluorophore from external quenchers. Such confinement limits rotational and vibrational freedom, thereby reducing non-radiative relaxation pathways and resulting in a marginally prolonged excited-state lifetime.[69] Moreover, the synthesized binary ensemble was

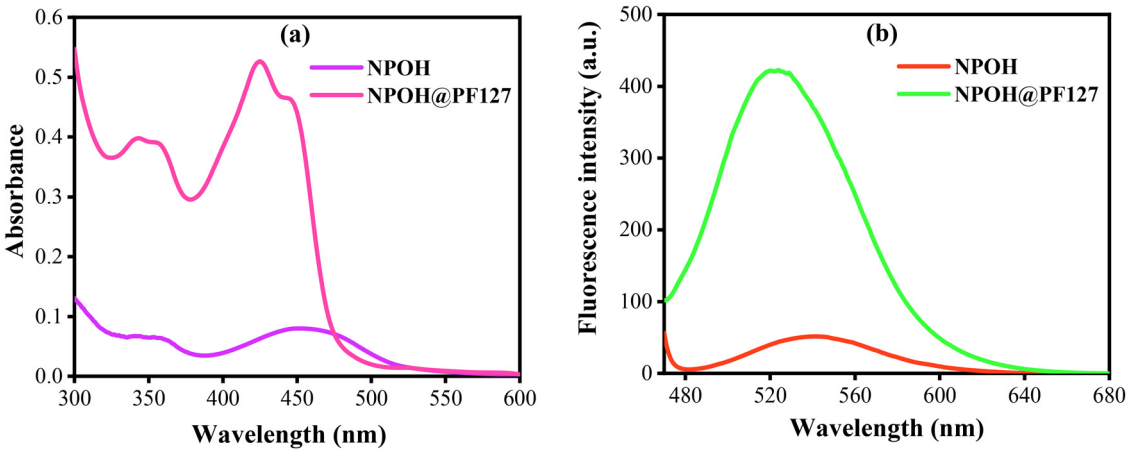

Fig. 4 (a) UV-vis absorption spectra and (b) fluorescence emission spectra of **NPOH** and **NPOH@PF127**.

found to be highly stable as the UV-vis absorption and fluorescence spectra of **NPOH@PF127** did not show any change in the presence of different concentrations of NaCl (20 μM to 200 μM) and at different time intervals (15 min to 8 h), as shown in Fig. S16 and S17.

3.3. Detection of CPS methyl using NPOH@PF127

The synthesized binary ensemble **NPOH@PF127** was utilized for the detection of perilous CPS methyl using optical spectroscopic techniques. As already discussed, **NPOH@PF127** displayed absorption bands at 446, 424, 356 and 343 nm in the UV-vis absorption spectrum. Upon the addition of 100 eq. of CPS methyl to the solution of **NPOH@PF127** (**NPOH** = 8 μM, **PF127** = 12 μM) in HEPES buffer (10 mM, pH = 7.0), no notable change was observed in the absorption spectrum of **NPOH@PF127** (Fig. S18). Further, UV-vis titrations of **NPOH@PF127** were performed with the progressive addition of increasing concentrations of CPS methyl, and the corresponding spectral changes are presented in Fig. S19. However, not much change was observed in the UV-vis spectrum of **NPOH@PF127** even after the addition of 300 eq. of CPS methyl.

In the emission spectrum, the emission peak at 524 nm due to **NPOH@PF127** was blue-shifted to 507 nm, along with a significant enhancement in intensity upon the addition of 100 eq. of CPS methyl to the solution of **NPOH@PF127** (**NPOH** = 20 μM, **PF127** = 30 μM) in HEPES buffer (10 mM, pH = 7.0) (Fig. 5). Further, to analyze the quantitative sensitivity of **NPOH@PF127** towards CPS methyl, fluorescence spectroscopic titrations were performed by sequential addition of increasing amounts of CPS methyl. As shown in Fig. 6, upon incremental addition of CPS methyl to the solution of **NPOH@PF127** (**NPOH** = 20 μM, **PF127** = 30 μM) in HEPES buffer (10 mM, pH = 7.0), a corresponding enhancement in emission intensity, along with a blue shift, was observed, and finally, saturation was observed at 1500 μM of CPS methyl. On applying the Benesi–Hildebrand equation to the fluorescence spectral titration data, the binding constant between **NPOH@PF127** and CPS methyl was calculated to be 7.19×10^3 M^{-1}.[57,70]

The limit of detection (LOD) value of **NPOH@PF127** towards CPS methyl calculated using the formula LOD = $3\sigma/s$ ('σ' is the standard deviation of measurements obtained from seven blank replicates and 's' is the slope of the standard calibration curve of fluorescence spectral titration data) was found to be 1.28 μM.[71,72] Moreover, the linear detection range of the proposed sensor **NPOH@PF127** towards CPS methyl was found to be 4.22–1500 μM, which is defined as the concentration interval extending from the limit of quantification (LOQ = 3.3 × LOD) up to the point at which the maximum change in the emission spectrum was observed.

Real samples are complex and contain a variety of other substances, along with the analyte of interest; therefore, for any sensing system to be efficient, it should be able to detect a particular analyte in the presence of various possible interferents. To check the selectivity of **NPOH@PF127** towards CPS

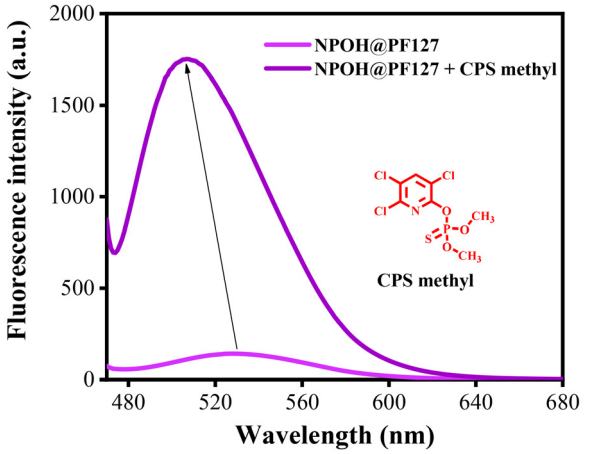

Fig. 5 Fluorescence emission spectrum of **NPOH@PF127** in the presence of CPS methyl.

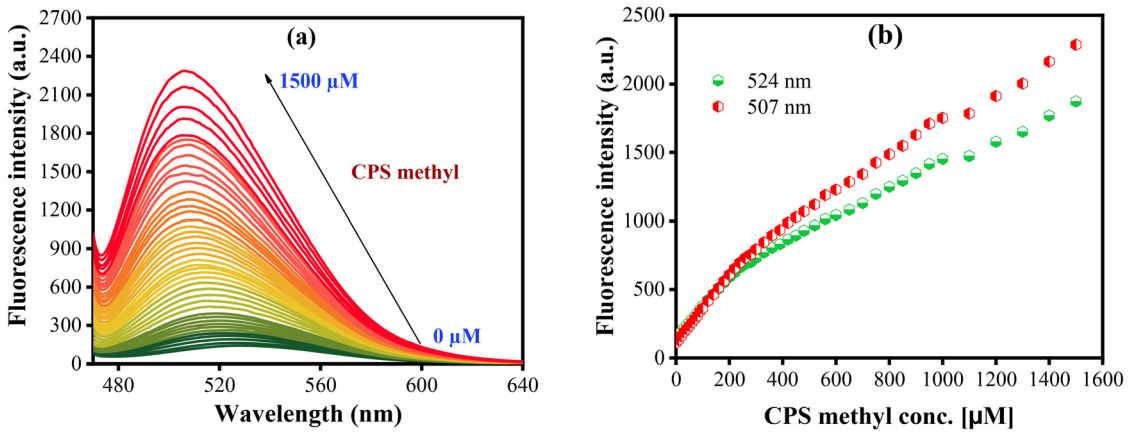

Fig. 6 (a) Fluorescence spectra of **NPOH@PF127** at various concentrations of CPS methyl. (b) Plot of the fluorescence intensity of **NPOH@PF127** at 524 and 507 nm *versus* the concentration of added CPS methyl.

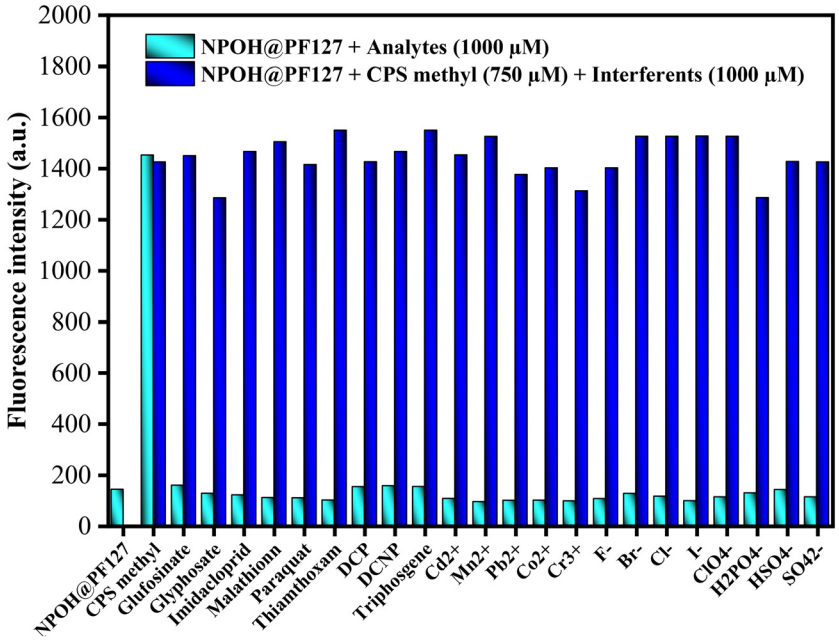

Fig. 7 Fluorescence interference graph of **NPOH@PF127** and **NPOH@PF127** + CPS methyl in the presence of various possible interferents.

methyl, interference from various other pollutants (glufosinate, glyphosate, imidacloprid, malathion, paraquat, thiamethoxam, DCP, DCNP, triphosgene, Cd^{2+}, Mn^{2+}, Pb^{2+}, Co^{2+}, Cr^{3+}, F^{-}, Cl^{-}, Br^{-}, I^{-}, ClO_4^{-}, $H_2PO_4^{-}$, HSO_4^{-} and SO_4^{2-}) was assessed by observing changes in the emission spectrum of **NPOH@PF127** in the presence of the aforementioned possible interferents both in the presence and absence of CPS methyl. Fig. 7 reveals that none of the interferents caused discernible changes in the emission spectrum of **NPOH@PF127**, indicating the high selectivity of **NPOH@PF127** towards CPS methyl.

3.4. Detection of erythrosine B using NPOH@PF127

UV-vis and fluorescence spectroscopic techniques were utilized to evaluate the sensing potential of **NPOH@PF127** towards erythrosine B. The addition of erythrosine B to the solution of **NPOH@PF127** (**NPOH** = 8 μM, **PF127** = 12 μM) in HEPES buffer (10 mM, pH = 7.0) led to the enhancement in intensity of absorption bands at 446, 424, 356 and 343 nm and a new band appeared around 525 nm due to the own absorption of erythrosine B (Fig. S20). Further, UV-vis titrations of **NPOH@PF127** were carried out with increasing amounts of erythrosine B, and the results are displayed in Fig. S21. In the emission spectrum, significant quenching in emission intensity at 524 nm, along with appearance of new peak at 567 nm corresponding to the emission of erythrosine B itself, was observed upon the addition of erythrosine B to the solution of **NPOH@PF127** (**NPOH** = 60 μM, **PF127** = 90 μM) in HEPES buffer (10 mM, pH = 7.0) (Fig. 8). Further, the emission spectrum of **NPOH@PF127** was recorded with continual addition of rising concentrations of erythrosine B. Continuous addition of erythrosine B to the solution of **NPOH@PF127** led to a

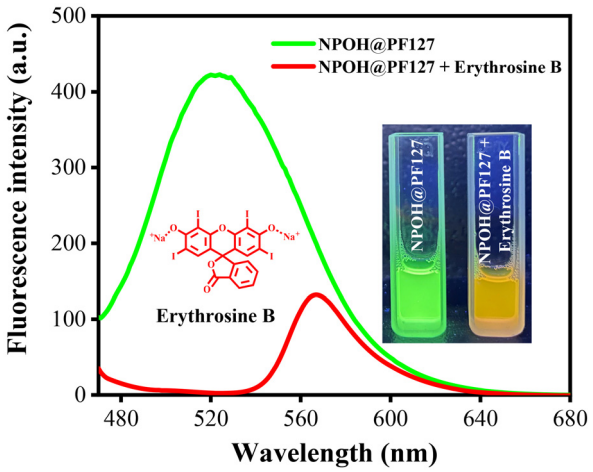

Fig. 8 Emission spectrum of **NPOH@PF127** in the presence of erythrosine B; inset: fluorescence color change of **NPOH@PF127** in the presence of erythrosine B.

gradual decrease in emission intensity and finally saturation was observed at 138 μM of erythrosine B (Fig. 9).

The Benesi–Hildebrand equation[57,70] was applied to fluorescence spectral titration data to calculate the binding constant between **NPOH@PF127**, which was found to be 5.06×10^4 M^{-1}. The LOD value and linear detection range of **NPOH@PF127** towards erythrosine B were determined to be 0.18 μM and 0.59–138 μM, respectively.[71,72]

To ensure the applicability of **NPOH@PF127** in real samples, the selectivity of **NPOH@PF127** towards erythrosine B in the presence of various possible interferents needs to be assessed. Therefore, anti-interference experiments were con-

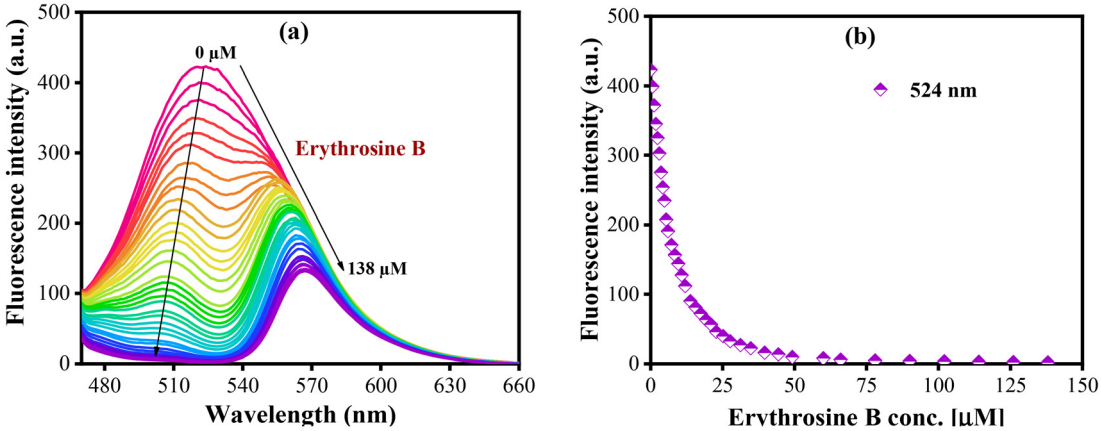

Fig. 9 (a) Fluorescence spectra of **NPOH@PF127** at various concentrations of erythrosine B. (b) Plot of the fluorescence intensity of **NPOH@PF127** at 524 nm *versus* the concentration of added erythrosine B.

ducted to evaluate the sensing potential of **NPOH@PF127** towards other food dyes, food additives, various metal ions and anions. Consequently, emission spectra of **NPOH@PF127** in the presence of food dyes (Allura red, amaranth, methylene blue, methyl orange), food additives (glucose, sucrose, maltose, lactose, citric acid, ascorbic acid), metal ions (Cd^{2+}, Mn^{2+}, Pb^{2+}, Co^{2+}, and Cr^{3+}) and anions (F^-, Cl^-, Br^-, I^-, ClO_4^-, $H_2PO_4^-$, HSO_4^-, and SO_4^{2-}) were recorded both in the absence and presence of erythrosine B (Fig. 10). None of these interferents interfered in the sensing of erythrosine B as indicated by no noticeable changes in the emission spectrum of **NPOH@PF127** and **NPOH@PF127** + erythrosine B in the presence of these interferents. Thus, anti-interference experiments revealed the highly selective nature of **NPOH@PF127** towards erythrosine B and indicate its effectiveness in real-world samples.

3.5. Mechanism

As already discussed, a significant enhancement in the emission intensity of **NPOH@PF127** was observed in the presence of CPS methyl. To understand the mechanism of interaction between **NPOH@PF127** and CPS methyl, FT-IR spectroscopy was utilized. However, the FT-IR spectrum of **NPOH@PF127** + CPS methyl was found to be quite similar to that of **NPOH@PF127**, indicating that no chemical interaction occurred on the surface of **NPOH@PF127** micelles (Fig. S22). Thus, the molecular interactions between **NPOH@PF127** and CPS methyl, causing changes in the emission spectrum of

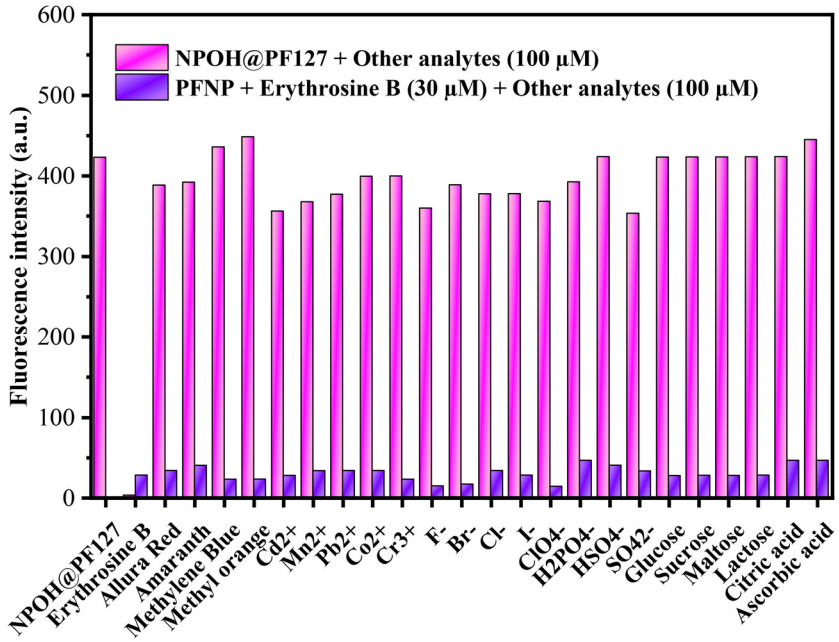

Fig. 10 Fluorescence interference graph of **NPOH@PF127** and **NPOH@PF127** + erythrosine B in the presence of various possible interferents.

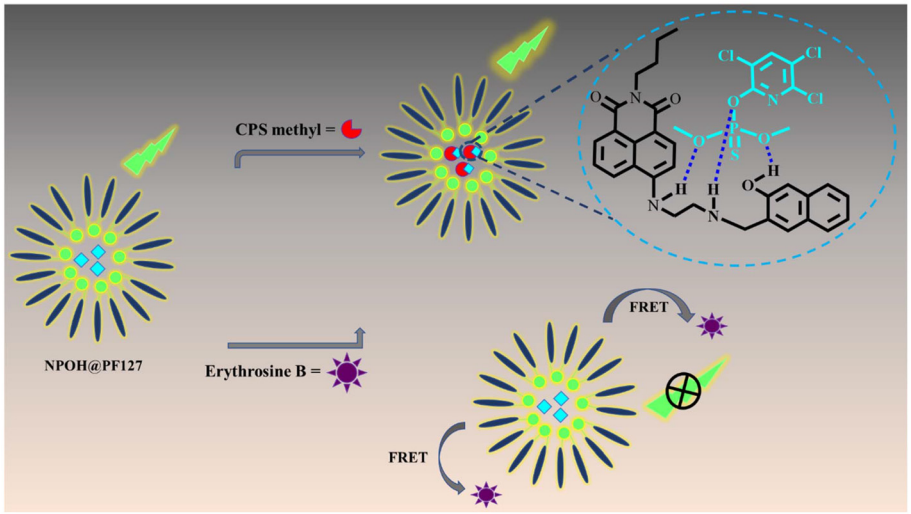

Fig. 11 Illustration of the plausible detection mechanism of CPS methyl and erythrosine B by **NPOH@PF127**.

NPOH@PF127 in the presence of CPS methyl, must have occurred within the micelles, involving **NPOH** and CPS methyl. Inside the polymeric micelles, oxygen atoms of CPS methyl might have interacted with the –NH and –OH hydrogens of **NPOH** *via* hydrogen bonding, which is supported by the observed increase in intensity and slight shift in the FT-IR bands corresponding to the O–H and N–H functional groups of **NPOH** upon the addition of CPS methyl (Fig. S23, Fig. 11).[3] Enhancement observed in the emission spectrum of **NPOH@PF127** in the presence of CPS methyl may be attributed to the hydrogen bonding-induced rigidity, leading to a reduction in the non-radiative decay and improved micellar microenvironment around **NPOH**.[73–75]

In the presence of erythrosine B, significant quenching was observed in the emission spectrum of **NPOH@PF127**. Usually, three types of mechanisms are considered responsible that cause quenching in the emission spectrum, including molecular interactions, inner filter effect (IFE) and fluorescence resonance energy transfer (FRET).[67,76] To gain insights into the molecular interactions between **NPOH@PF127** and erythrosine B, the FT-IR spectrum of **NPOH@PF127** + erythrosine B was compared with the FT-IR spectrum of **NPOH@PF127** alone, and it was found that both FT-IR spectra were completely identical; thus, no information about molecular interactions could be extracted with the help of FT-IR spectroscopy. Further, in FRET and IFE processes, upon excitation, the donor fluorophore exchanges energy with the acceptor chromophore with the same energy in resonance. For the FRET process to occur, the main criterion is the significant overlap between the emission spectrum of the fluorophore and the absorption spectrum of the acceptor.[76] In the present case, significant overlap exists between the emission spectrum of **NPOH@PF127** and the absorption spectrum of erythrosine B (Fig. S24), which is an ideal condition for the FRET mechanism to occur; thus the FRET mechanism might be held responsible for the quenching observed in the emission intensity of **NPOH@PF127** in the presence of erythrosine B. To validate the proposed mechanism, the fluorescence decay curves of **NPOH@PF127** and **NPOH@PF127** + erythrosine B were recorded, and the results are presented in Fig. S25. A significant decrease in the fluorescence lifetime of **NPOH@PF127** from 5.53 ns to 1.98 ns in the presence of erythrosine B confirmed the occurrence of a FRET mechanism responsible for the observed quenching in fluorescence intensity.[77] Other reasons responsible for the observed quenching in the emission intensity of **NPOH@PF127** in the presence of erythrosine B may include heavy-atom-induced intersystem crossing (ISC) due to the presence of four iodine atoms in erythrosine B and possible electron transfer, all of which create highly efficient non-radiative decay pathways.[78,79]

Further, as shown in Fig. 3, S26 & S27, the difference in the intensity of the binding energy peaks corresponding to C–C/C=C, C–O/C–N, N–H and C–OH indicated that these functional groups in **NPOH@PF127** might have chemically interacted with CPS methyl.[80] Moreover, the presence of various functional groups corresponding to CPS methyl and erythrosine B in XPS (Fig. S26 & S27) and EDX spectra (Fig. S28) of **NPOH@PF127** + CPS methyl and **NPOH@PF127** + erythrosine B also supported chemical interactions among **NPOH@PF127** and both analytes.

4. Analysis of real samples

Fluorescence spectroscopy was utilized for the detection of CPS methyl and erythrosine B in grape and watermelon juices using **NPOH@PF127**. Samples of grape and watermelon juices were prepared as per the procedure mentioned in the experimental section. The results of CPS methyl spiked (50, 800, 1500 μM) in grape juice and erythrosine B spiked (4, 15, 60 μM) in watermelon juice are displayed in Tables 1 and 2, respectively. For both samples, analysis was carried out in

Table 1 Determination of CPS methyl in grape juice using **NPOH@PF127**

		Found (μM)			Recovery (%)				
Sample name	Added (μM)	R1	R2	R3	R1	R2	R3	SD (μM)	RSD (%)
Grape juice	50	51.5	48.0	52.15	103.0	96.0	104.3	2.23	4.41
	800	805.6	808.0	816.0	100.7	101.0	102.0	5.45	0.67
	1500	1510.4	1513.5	1515.0	100.69	100.9	101.0	2.37	0.15

Table 2 Determination of erythrosine B in watermelon juice using **NPOH@PF127**

		Found (μM)			Recovery (%)				
Sample name	Added (μM)	R1	R2	R3	R1	R2	R3	SD (μM)	RSD (%)
Watermelon juice	5	5.1	4.8	5.3	102.0	96.62	105.0	0.21	4.20
	15	16.3	16.1	16.5	109.0	107.0	110.0	0.23	1.41
	60	65.3	60.4	60.2	108.8	100.7	100.4	2.86	4.61

triplicate, and excellent recoveries in the range of 96 to 110% were obtained with RSD values less than 5%. The standard deviation (SD) values calculated from the concentrations of analytes found in grape juice and watermelon juice are also displayed in Tables 1 and 2, respectively.

5. Comparison of the present sensor system, **NPOH@PF127**, with other reported sensors for CPS methyl and erythrosine B

The performance of the present sensor system, **NPOH@PF127**, was compared with other reported sensors in terms of the method of detection, concentration range, and LOD values for the sensing of CPS methyl and erythrosine B, and the results are summarized in Table S1. Compared to these literature reports, the present sensor system, **NPOH@PF127**, exhibited superior performance in terms of higher sensitivity for erythrosine B, enabled simultaneous detection of two analytes and wide detection window in terms of concentration.

6. Conclusion

In summary, we present a novel amide-functionalized **NPOH** fluorophore and its **PF127**-based micellar ensemble. The developed binary ensemble, **NPOH@PF127**, exhibited enhanced aqueous solubility and distinct fluorescence responsiveness. The probe shows clear spectral modulation toward CPS methyl and erythrosine B, governed by specific interaction pathways and FRET-assisted signalling, enabling reliable performance in real food matrices. The principal novelty of this work lies in encapsulating a 1,8-naphthalimide-derived amide sensor (**NPOH**) within a biocompatible micellar carrier (**PF127**) to achieve efficient signalling behaviour in aqueous media. Owing to its modular design, photostability and favourable dispersibility, the **NPOH@PF127** platform holds strong potential for future translation into practical formats, such as portable fluorescence strips, microfluidic sensing chips, and continuous monitoring setups for quality control environments in the food and beverage sector.

Author contributions

Nisha Jain: Conceptualization, data curation, formal analysis, visualization, writing – original draft. Navneet Kaur: Methodology, writing – review & editing, supervision, project administration.

Data availability

The data supporting this article have been included as part of the supplementary information (SI). Supplementary information is available. See DOI: https://doi.org/10.1039/d5lp00287g.

Conflicts of interest

The authors declare no competing interests.

Acknowledgements

The authors are grateful to DST INSPIRE (IF200020) for the financial assistance and are greatly thankful to SAIF, Panjab University, Chandigarh, for DLS, HRTEM, FESEM, PXRD, NMR and mass spectral studies.

References

1 Z.-H. Xu, J. Liu, B. Li, J.-K. Wang, X. Zeng, Z.-J. Chen, S. Hongsibsong, W. Huang, H.-T. Lei, Y. M. Sun and Z.-L. Xu, *Biosensors*, 2022, **12**, 1006.
2 G. L. Tadesse and T. Kasa, *Adv. Life Sci. Technol.*, 2017, **55**, 13–22.
3 M. Kumar, A. Dhiman, G. Singh, N. Kaur and N. Singh, *Anal. Chim. Acta*, 2025, **1336**, 343488.
4 X. Hua, G. Qian, J. Yang, B. Hu, J. Fan, N. Qin, G. Li, Y. Wang and F. Liu, *Biosens. Bioelectron.*, 2010, **26**, 189–194.
5 G. Qian, L. Wang, Y. Wu, Q. Zhang, Q. Sun, Y. Liu and F. Liu, *Food Chem.*, 2009, **117**, 364–370.
6 S. I. S. Al-Hawary, A. O. Bali, S. Askar, H. A. Lafta, Z. J. Kadhim, B. Kholdorov, Y. Riadi, R. Solanki, Q. I. Kadhem and Y. F. Mustafa, *Microchem. J.*, 2023, **189**, 108540.
7 W. Ahmad, E. H. Aljuhani, H. Alwael, E. A. Assirey, H. M. Nassef and M. S. El-Shahawi, *J. Food Compos. Anal.*, 2023, **117**, 105110.
8 S. Firdoushi, A. H. M. T. Ahmed, I. Bhattacharjee, S. Dasgupta, H. Ghosh, D. Biswas, R. Bandyopadhyay and B. Tudu, *Food Hum.*, 2025, **4**, 100586.
9 G. E. Uwaya and K. Bisetty, *Inorg. Chem. Commun.*, 2025, **178**, 114512.
10 C. Zhang, Y. J. Wu, S. F. Jin and H. Yang, *Anal. Methods*, 2013, **5**, 3089–3095.
11 E. Anli, N. Vural, H. Vural and Y. Gucer, *J. Inst. Brew.*, 2007, **113**, 213–218.
12 H. Li, M. M. Hassan, Z. He, S. A. Haruna, Q. Chen and Z. Ding, *LWT–Food Sci. Technol.*, 2022, **167**, 113804.
13 M. D. Carlo, M. Mascini, A. Pepe, D. Compagnone and M. Mascini, *J. Agric. Food Chem.*, 2002, **50**, 7206–7210.
14 H. Li, J. Li, Q. Xu and X. Hu, *Anal. Chem.*, 2011, **83**, 9681–9686.
15 W. Wei, X. Zong, X. Wang, L. Yin, Y. Pu and S. Liu, *Food Chem.*, 2012, **135**, 888–892.
16 K. Tuovinen, M. Kolehmainen and H. Paakkanen, *Anal. Chim. Acta*, 2001, **429**, 257–268.
17 S. N. Sinha, R. Pal, A. Dewan, M. M. Mansuri and H. N. Saiyed, *Int. J. Mass Spectrom.*, 2006, **253**, 48–57.
18 D. B. Roll and F. J. Biros, *Anal. Chem.*, 1969, **41**, 407–411.
19 Q. Chen and Y. Fung, *Electrophoresis*, 2010, **31**, 3107–3114.
20 M. A. Martínez, S. Ballesteros, C. S. de la Torre, A. Sanchiz, E. Almarza and A. García-Aguilera, *J. Anal. Toxicol.*, 2004, **28**, 609–615.
21 J. F. Liu, T. Wen, N. B. Li and H. Q. Luo, *Sens. Actuators, B*, 2011, **160**, 1128–1135.
22 Y.-Y. Ma, Z.-J. Wang and D.-J. Qian, *Talanta*, 2021, **230**, 122311.
23 X. Chen, J. Xu, L. Zhang, N. Bi, J. Gou, Y. Li, T. Zhao and L. Jia, *Food Chem.*, 2024, **439**, 138095.
24 M. Li, L. Jia, X. Chen, Y. Li, D. Zhao, L. Zhang, T. Zhao and J. Xu, *Sens. Actuators, B*, 2024, **407**, 135491.
25 J. Xu, S. Guo, L. Jia, T. Zhu, X. Chen and T. Zhao, *Chem. Eng. J.*, 2021, **416**, 127741.
26 T. Yang, S. Feng, Y. Lu, C. Yin and J. Wang, *J. Sep. Sci.*, 2016, **39**, 2388–2395.
27 R. Kaur and N. Kaur, *Dyes Pigm.*, 2017, **139**, 310–317.
28 X. Yue, C. Zhu, R. Gu, J. Hu, Y. Xu, S. Ye and J. Zhu, *Foods*, 2022, **11**, 3336.
29 R. Chadha, A. Das, J. Lobo, V. O. Meenu, A. Paul, A. Ballal and N. Maiti, *Colloids Surf., A*, 2022, **641**, 128558.
30 S. Wang, Y. Kang, L. Wang, H. Zhang, Y. Wang and Y. Wang, *Sens. Actuators, B*, 2013, **182**, 467–481.
31 W. Li, H. Zhou, M. A. H. Nawaz, N. Niu, N. Yang, J. Ren and C. Yu, *Anal. Methods*, 2020, **12**, 5353–5359.
32 N. Kaur, R. Kaur, R. Kaur and S. Rana, *Inorg. Chem. Commun.*, 2021, **129**, 108648.
33 F. Gai, M. Fan, X. Yang, C. Hao, Y. Ao, C. Duan, Y. Liu and Q. Huo, *J. Colloid Interface Sci.*, 2018, **519**, 224–231.
34 F. Gai, L. Yin, M. Fan, L. Li, J. Grahn, Y. Ao, X. Yang, X. Wu, Y. Liu and Q. Huo, *J. Colloid Interface Sci.*, 2018, **514**, 357–363.
35 F. Gai, L. Li, Y. Yu, Z. Han, L. Jin, Y. Ao, Y. Liu and Q. Huo, *J. Colloid Interface Sci.*, 2018, **529**, 531–537.
36 A. R. Alzahrani, *Green Process. Synth.*, 2023, **12**, 20230126.
37 N. Molupe, B. Babu, D. O. Oluwole, E. Prinsloo, L. Gai, Z. Shen, J. Mack and T. Nyokong, *J. Porphyrins Phthalocyanines*, 2020, **24**, 973–984.
38 X. Xie, G. Mistlberger and E. Bakker, *Anal. Chem.*, 2013, **85**, 9932–9938.
39 B. Pucelik, L. G. Arnaut, G. Stochel and J. M. Dąbrowski, *ACS Appl. Mater. Interfaces*, 2016, **8**, 22039–22055.
40 V. P. Torchilin, *Pharm. Res.*, 2006, **24**, 1–16.
41 X. Ye, J. Zhang, H. Chen, X. Wang and F. Huang, *ACS Appl. Mater. Interfaces*, 2014, **6**, 5113–5121.
42 Z. Wei, J. Hao, S. Yuan, Y. Li, W. Juan, X. Sha and X. Fang, *Int. J. Pharm.*, 2009, **376**, 176–185.
43 N. U. Khaliq, J. Lee, S. Kim, D. Sung and H. Kim, *Pharmaceutics*, 2023, **15**, 2102.
44 S. M. Tawfik, S. Azizov, M. R. Elmasry, M. Sharipov and Y. I. Lee, *Nanomaterials*, 2021, **11**, 70.
45 N. Jain and N. Kaur, *Coord. Chem. Rev.*, 2022, **459**, 214454.
46 X. Li, Y. Zhou, Y. Zhang and Y. A. Son, *Mol. Cryst. Liq. Cryst.*, 2015, **622**, 84–93.
47 J.-C. Qin, J. Yan, B.-D. Wang and Z.-Y. Yang, *Tetrahedron Lett.*, 2016, **57**, 1935–1939.
48 M. Mehta, W. Skinner, B. Gardner, S. Mosca, F. Palombo, P. Matousek and N. Stone, *ACS Omega*, 2025, **10**, 4588–4598.
49 X. Wang, Y. Wang, L. Yin, Q. Zhang and S. Wang, *RSC Adv.*, 2022, **12**, 10395–10400.
50 M. I. Henderson, Y. Eygeris, A. Jozic, M. Herrera and G. Sahay, *Mol. Pharmaceutics*, 2022, **19**, 4275–4285.
51 E. V. Kuznetsova, N. M. Kuznetsov, K. T. Kalinin, P. V. Lebedev-Stepanov, A. A. Novikov and S. N. Chvalun, *Colloid J.*, 2025, **84**, 704–714.
52 J. K. Lim, S. P. Yeap, H. X. Che and S. C. Low, *Nanoscale Res. Lett.*, 2013, **8**, 381.
53 R.-S. Juang, K.-S. Wang, Y.-W. Cheng, W.-E. Wu, Y.-H. Lin, R.-J. Jeng, L.-Y. Huang, M.-C. Yang, S.-H. Liu and T.-Y. Liu, *Spectrochim. Acta, Part A*, 2022, **279**, 121475.

54 N. Akhlaghi and G. Najafpour-Darzi, *J. Mol. Liq.*, 2024, **400**, 124489.
55 Y. Wang, L. Nie, Y. Hua, L. Gong, X. Qiu and H. Guo, *Spectrochim. Acta, Part A*, 2023, **292**, 122431.
56 Jyoti, Deepeka, P. Kaur, V. Kumar, K. Tikoo, S. Rana and S. Singhal, *Anal. Chim. Acta*, 2023, **1240**, 340753.
57 N. Jain and N. Kaur, *Food Chem.*, 2025, **485**, 144546.
58 J. Cao, Z. Cheng, L. Kang, M. Chu, D. Wu, M. Li, S. Xie and R. Wen, *Mater. Lett.*, 2017, **207**, 190–194.
59 C. Shen, J. Zhu, J. Song, J. Wang, B. Shen, H. Yuan and X. Li, *Drug Dev. Ind. Pharm.*, 2020, **46**, 1100–1107.
60 M. Akrami-Hasan-Kohal, A. Chouchou, S. Blanquer and T. Sharkawi, *Int. J. Pharm.: X*, 2024, **7**, 100230.
61 P. Gu, X. Xu, F. Zhou, T. Zhao, G. Ye, G. Liu, Q. Xu, J. Ge, Q. Xu and J. Lu, *Chin. J. Chem.*, 2014, **32**, 205–211.
62 P. Gu, X. Xu, F. Zhou, T. Zhao, G. Ye, G. Liu, Q. Xu, J. Ge, Q. Xu and J. Lu, *Chin. J. Chem.*, 2014, **32**, 205–211.
63 K. Gayen, S. Paul, S. Hazra and A. Banerjee, *Langmuir*, 2021, **37**, 9577–9587.
64 S. Dhar, D. K. Rana and S. C. Bhattacharya, *Colloids Surf., A*, 2012, **402**, 117–126.
65 S. Sreejith, J. Joseph, M. Lin, N. V. Menon, P. Borah, H. J. Ng, Y. X. Loong, Y. Kang, S. W.-K. Yu and Y. Zhao, *ACS Nano*, 2015, **9**, 5695–5704.
66 W.-C. Wu, C.-Y. Chen, Y. Tian, S.-H. Jang, Y. Hong, Y. Liu, R. Hu, B. Z. Tang, Y.-T. Lee, C.-T. Chen, W.-C. Chen and A. K. Y. Jen, *Adv. Funct. Mater.*, 2010, **20**, 1413–1423.
67 Y. Bo, J. Fan, S. Yan, M. Ding, J. Liu, J. Peng and L. Ding, *Sens. Actuators, B*, 2019, **295**, 168–178.
68 N. Jain and N. Kaur, *Colloids Surf., A*, 2024, **693**, 134092.
69 Y. Lu, P. Jabbari, A. Mukhamedshin and A. V. Zvyagin, *Adv. Drug Delivery Rev.*, 2025, **218**, 115521.
70 H. A. Benesi and J. H. Hildebrand, *J. Am. Chem. Soc.*, 1949, **71**, 2703–2707.
71 D. Kumar and N. Kaur, *Carbohydr. Polym. Technol. Appl.*, 2024, **7**, 100500.
72 G. L. Long, *Anal. Chem.*, 1983, **55**, 712A–724A.
73 Z. Zhang, Y. Zhang, P. Jiang, G. Lu, Z. Chen, H. Yu and Y. Qi, *Chem. – Eur. J.*, 2025, **31**, e202404484.
74 H.-Y. Zhang, M. Zhang, H. Zhuo, H.-Y. Yang, B. Han, Y.-H. Zheng, H. Wang, H. Lin, S.-L. Tao, C.-J. Zheng and X.-H. Zhang, *Chem. Sci.*, 2024, **15**, 14651–14659.
75 F. Ma, G. Zhao, Y. Zheng, F. He, K. Hasrat and Z. Qi, *ACS Appl. Mater. Interfaces*, 2020, **12**, 1179–1189.
76 K. Shanmugaraj and S. A. John, *New J. Chem.*, 2018, **42**, 7223–7229.
77 K. Anusuyadevi and S. Velmathi, *Anal. Chim. Acta*, 2023, **1239**, 340678.
78 N. Ibrayev, E. Seliverstova, R. Valiev, A. Aymagambetova and D. Sundholm, *Phys. Chem. Chem. Phys.*, 2024, **26**, 25986–25993.
79 A. Mukherjee, J. Feist and K. Börjesson, *J. Am. Chem. Soc.*, 2023, **145**, 5155–5162.
80 C. Xu, J. Wang, L. Wan, J. Lina and X. Wang, *J. Mater. Chem.*, 2011, **21**, 10463–10471.